An Anomalous Genesis Potential Index for MJO Modulation of Tropical Cyclones

BIN WANG

Department of Atmospheric Sciences, International Pacific Research Center, and Atmosphere–Ocean Research Center, University of Hawai'i at Mānoa, Honolulu, Hawaii, and Earth System Modeling Center, Nanjing University of Information Science and Technology, Nanjing, China

JA-YEON MOON

Department of Atmospheric Sciences, International Pacific Research Center, and Atmosphere–Ocean Research Center, University of Hawai'i at Mānoa, Honolulu, Hawaii

(Manuscript received 18 October 2016, in final form 19 January 2017)

ABSTRACT

Modulation of tropical cyclone (TC) genesis by the Madden–Julian oscillation (MJO) has been quantitatively diagnosed by using a climatological genesis potential index (GPI). Analysis of TC genesis during November–April of 1979–2014 indicates the most effective factors controlling intraseasonal TC genesis are 850-hPa relative vorticity weighted by the Coriolis parameter $f\zeta_{r850}$ and 500-hPa vertical motion ω_{500}. The total vertical wind shear and maximum potential intensity are unimportant, and the role of 600-hPa relative humidity is greatly represented by ω_{500}. The MJO modulates TC genesis primarily through changing low-level vorticity induced by its Rossby wave gyres and meridional shears of equatorial zonal winds. A new intraseasonal GPI (ISGPI) is proposed to quantify the MJO's modulation of TC genesis. The ISGPI significantly improves representation of intraseasonal variation of TC genesis in the tropics and in each subregion of the southern Indian Ocean, Australian monsoon, and South Pacific. In the hot spots of the Southern Hemisphere TC genesis zone, the probability of TC genesis can differ by a factor of 5–19 as a result of MJO modulation. The results suggest that the large-scale factors controlling TC genesis may vary with different time scales, and the climatological GPI may not be quite applicable for diagnoses of climate variability and future change of TC genesis potential. To simulate realistic impacts of the MJO on TC genesis, general circulation models must reproduce not only realistic eastward propagation but also the MJO low-level circulation structure. Application of the new ISGPI may have a large potential to improve dynamical subseasonal prediction of TC genesis.

1. Introduction

Statistically, the MJO (Madden and Julian 1971, 1972) was defined as the spectral components within zonal wavenumbers 1–3 and having periods 30–80 days in the wavenumber–frequency spectrum of outgoing longwave radiation (OLR) and 850-hPa zonal winds (Waliser et al. 2009). From a dynamical standpoint, the MJO can be defined as a tropical, planetary-scale circulation system (coupled with a multiscale convective complex) moving eastward slowly over the Indo–Pacific warm pool with a rearward-tilted vertical motion and a coupled Kelvin–Rossby wave structure (Wang and Chen 2016).

The MJO is the dominant mode of tropical atmospheric intraseasonal variability (ISV) and a major source of global predictability on the subseasonal time scale (Waliser 2011). The MJO is also a fundamental regulator for extreme and high-impact weather events such as tropical storms, flooding, droughts, heavy snowstorms, heat waves, cold surges, wild fire, hazes, tornado, and hail days (Zhang 2013; Wang and Moon 2017).

Previous empirical studies have qualitatively established the impacts of MJO on tropical cyclone (TC)

International Pacific Research Center Publication Number 1239, School of Ocean and Earth Science and Technology Publication Number 9957, and Nanjing University of Information Science and Technology Earth System Modeling Center Publication Number 153.

Corresponding author e-mail: Dr. Ja-Yeon Moon, mjy1011@gmail.com

DOI: 10.1175/JCLI-D-16-0749.1

activity in the global ocean since late 1980s. Over the western North Pacific, enhanced TC activity and rapid intensification were found to occur during the convective phase of MJO (Nakazawa 1988; Liebmann et al. 1994; Wang and Zhou 2008; Kim et al. 2008; Li and Zhou 2013). Similar modulation of TC frequency and development during the MJO convective and westerly phases were found in the northern Indian Ocean (Liebmann et al. 1994; Kikuchi and Wang 2010; Krishnamohan et al. 2012), the eastern North Pacific (Molinari et al. 1997; Maloney and Hartmann 2000a; Aiyyer and Molinari 2008), the Gulf of Mexico and North Atlantic (Maloney and Hartmann 2000b; Barrett and Leslie 2009), the Australian region (Hall et al. 2001), the southern Indian Ocean (Bessafi and Wheeler 2006; Ramsay et al. 2012), and the South Pacific (Chand and Walsh 2010). When MJO convection is enhanced in the Indian Ocean, an enhanced TC activity in the remote Atlantic main development region was also noticed (Klotzbach 2010; Ventrice et al. 2011). In the aforementioned studies, a number of large-scale environmental conditions associated with MJO have been recognized as favorable factors to enhance TC genesis (TCG) including the low-level cyclonic vorticity (Liebmann et al. 1994; Hall et al. 2001; Bessafi and Wheeler 2006; Wang and Zhou 2008), low-level westerly anomalies (Maloney and Hartmann 2000a), reduced total vertical wind shear (Bessafi and Wheeler 2006), and upper-level divergence (Barrett and Leslie 2009). TC development is often observed in the region to the west and poleward side of the enhanced MJO convection (Kikuchi and Wang 2010; Krishnamohan et al. 2012; Jiang et al. 2012).

Quantitative diagnosis of the contribution of large-scale factors on TCG was attempted first by Camargo et al. (2009), who applied the genesis potential index (GPI) established by Emanuel and Nolan (2004) (ENGPI):

$$\mathrm{ENGPI} = |10^5\eta|^{3/2}\left(\frac{H}{50}\right)^3\left(\frac{V_{\mathrm{pot}}}{70}\right)^3(1+0.1V_{\mathrm{shear}})^{-2}, \qquad (1)$$

where η is the absolute vorticity at 850 hPa (s^{-1}), H is the relative humidity at 600 hPa (%), V_{pot} is the maximum potential intensity ($m\,s^{-1}$), and V_{shear} is the magnitude of the total vertical wind shear between 200 and 850 hPa ($m\,s^{-1}$). Among the four influential factors, Camargo et al. (2009) found the midlevel relative humidity makes the largest and primary contribution to the TCG. They also found that the ENGPI captures MJO modulation of TCG frequency to a lesser degree than its capture of the climatological annual cycle of genesis. They speculated that this may be indicative of the importance of precursory disturbances, which was not well captured by the ENGPI. Although the midlevel humidity anomalies make the largest contribution to ENGPI, it may not be the root cause for MJO modulation as these thermodynamic anomalies and the large-scale circulation anomalies are interactive with convection. The increased moisture in the midlevel comes mainly from the moisture convergence induced by the low-frequency wave and boundary dynamics and implemented by upward turbulent transport of the surface entropy fluxes. In addition, although ENGPI reproduces the annual cycle of the TCG frequency very well (Camargo et al. 2007), it may not represent accurately the major processes by which the MJO affects the intraseasonal variations of the TCG frequency because the ENGPI was derived using climatological TCG data. Therefore, it remains an open issue as to how MJO exerts its large-scale control on TCG.

So far, an optimum quantitative expression of TCG potential on an intraseasonal time scale has not been established. Such a quantitative measure, however, will be very useful for pinpointing the mechanisms by which the MJO regulates TCG and can provide a useful tool for subseasonal prediction of TCG potential using the dynamical model-predicted large-scale fields.

The main endeavor of this study is to establish such an optimum expression linking MJO anomalies to TCG frequency anomaly. This effort starts from identification of major factors associated with MJO that affect the global TCG potential during austral summer from November to the next April when the MJO has the largest amplitude and most systematic eastward propagation (section 3). With the knowledge and understanding gained, a new TC genesis potential index, called intraseasonal GPI (ISGPI), will be proposed. Section 4 discusses the mechanism by which MJO regulates TCG. The applicability of ISGPI and its performance in reproducing observed intraseasonal TCG frequencies are evaluated in comparison with the ENGPI in section 5. The last section summarizes the main points and discusses implications of the present results.

2. Datasets and methodology

a. Datasets

The data used in the present study include daily variables derived from the European Centre for Medium-Range Weather Forecasts (ECMWF) interim reanalysis (ERA-Interim; Dee et al. 2011) from 1979 to 2014. Horizontal resolution is reduced to 2.5° × 2.5° in longitude and latitude. Daily OLR from the National Oceanic and Atmospheric Administration (NOAA), with a horizontal resolution of 2.5° × 2.5° from 1979 to 2014 (Liebmann and Smith 1996), is used as a proxy to depict

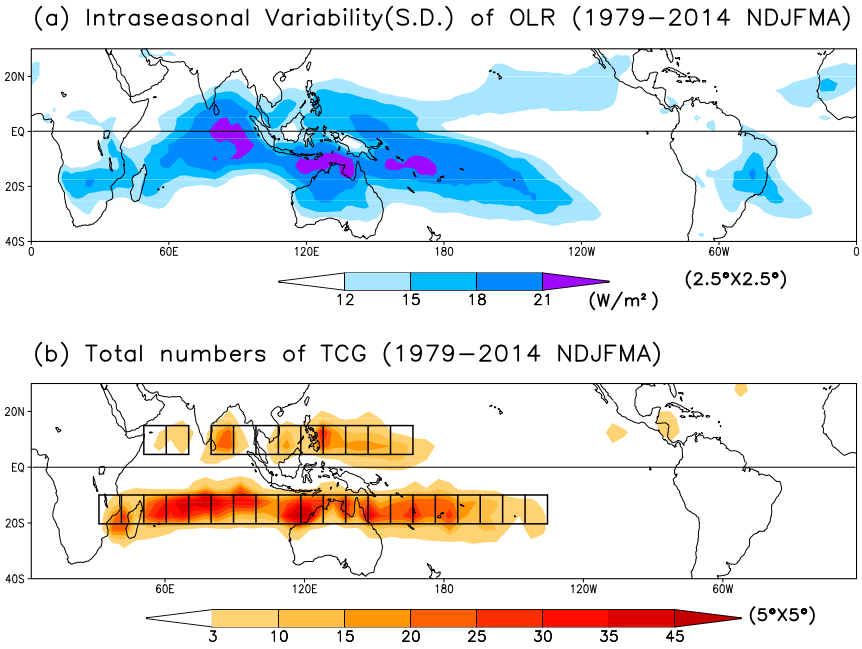

FIG. 1. (a) The 20–70-day intraseasonal variability (std dev) of OLR and (b) total numbers of TCG during austral summer (NDJFMA) of 1979–2014. Boxes indicate the selected 10° × 10° locations of TCG for stepwise regression analysis.

convection in the tropics. TC datasets are downloaded from International Best Track Archive for Climate Stewardship (IBTrACS; http://www.ncdc.noaa.gov/ibtracs), version 3 release 6 (v03r06), from 1979 to 2014 (Knapp et al. 2010). TC genesis occurs when it achieves a maximum sustained wind speed of 34 kt ($17\,m\,s^{-1}$). The present study will focus on the austral summer tropical cyclone season, and it is defined as November through the next April (NDJFMA). The MJO is defined as 20–70-day anomalies obtained by applying the Lanczos bandpass filter (Duchon 1979) to the daily datasets.

b. An OLR MJO index for austral summer season

Wheeler and Hendon (2004) used a real-time multivariate MJO (RMM) index [using OLR and 850- and 200-hPa zonal winds (U850 and U200)] to monitor all-year-round MJO. To investigate how MJO evolution affects TCG during austral summer (NDJFMA), we attempted a simple OLR index. As shown in Fig. 1, during NDJFMA the major MJO OLR variabilities are shifted to the Southern Hemisphere (SH) mostly between the equator and 20°S. The TCG also primarily occurs between 10° and 20°S. An austral summer MJO index is constructed using the combination of the first two leading empirical orthogonal function (EOF) modes of 20–70-day-filtered OLR anomaly between 0° and 20°S. The latitude range is selected as 0°–20°S because it covers both the major MJO variability bands and TCG bands very well. The resulting two leading EOFs explain 11.2% and 10.3% of the total integrated OLR variance, respectively.

The MJO evolution is described by eight phases in a similar way as in Wheeler and Hendon (2004). For each phase a composite is made by using the days when the amplitude of MJO index is greater than 1.0 [i.e., $(PC1^2 + PC2^2)^{1/2} \geq 1.0$]. Figure 2 shows the eight phase composite OLR anomalies and TCG anomalies. The OLR anomalies are more symmetric about the equator over the Indian Ocean and become asymmetric passing through Indonesia and Australia (from phase 6) toward the South Pacific, while the TCG is obviously equatorially asymmetric with major genesis regions located in the SH.

c. Method for deriving intraseasonal TC genesis potential index

Since the TCG frequency is very small on an individual day and at each 10° × 10° grid, we examine the genesis frequency at eight composite MJO phases because each composite phase consists of roughly 400–500 days, forming a sample member containing many TCG cases (Fig. 2). Spatially, the TCG occurs mainly in two latitude bands, 10°–20°S and 5°–15°N, and thus we selected 10° × 10° boxes along the two latitude bands. Figure 1b shows the distribution of the selected boxes used to form the statistical samples for both TCG

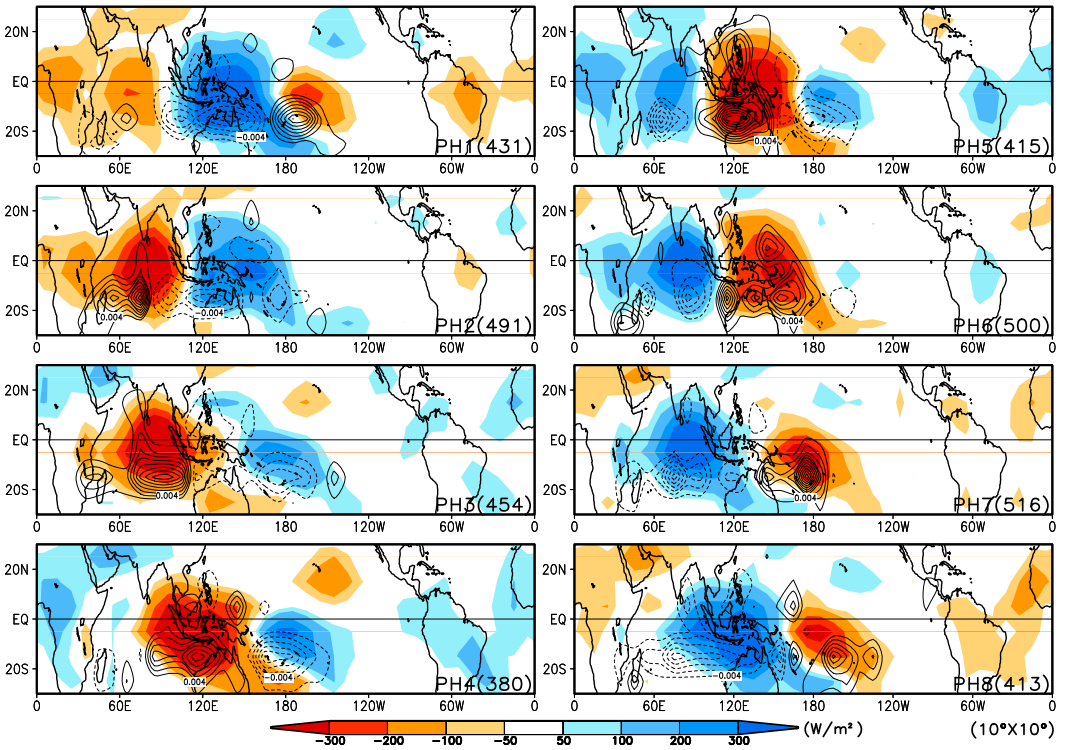

FIG. 2. Eight phase composite anomalies of intraseasonal OLR (shading) and TCG frequency (contour; TC number per day) associated with MJO evolution during austral summer (NDJFMA) of 1979–2014. The numbers in parentheses at the bottom-right corner indicate the total occurrence days of each MJO phase with the amplitude greater than 1.0. MJO index is obtained by the combination of first two leading EOF modes using horizontal distribution (20°S–0°, 0°–360°) of NDJFMA intraseasonal OLR anomaly.

frequency and MJO anomalies. Some of the boxes are located in the regions where the number of TCs is weaker than the other regions. Sensitivity tests including or removing the weaker TC boxes result in slightly higher correlation between TCG frequency and MJO anomalies (the complex correlation coefficient ranging 0.82–0.83). However, since increase of the sample size of TCGs and application to the global oceans are desirable, we have included every box of TCG. There are a total of 31 boxes, and the sample size used to compute the correlation coefficient is $31 \times 8 = 248$. As such, the averaged TCG frequency in each of the $10° \times 10°$ boxed areas is large enough to make meaningful statistics.

We used stepwise linear regression and the F test to select the factors and to construct the best multivariable, linear regression equation. The stepwise regression selects contributing factors in a sequential order by maximizing the regressed fractional variance at each step (Efroymson 1960). The Fisher's (F) test was used to test the significance of a new factor at each step in terms of the significance of its contribution to increase of the regressed variance. At the first step the factor having the highest correlation with TCG frequency is selected. At the second step the "newly" selected factor allows for yielding a maximum complex correlation coefficient by its combination with the selected factor. This process continues until no statistically significant factors can be selected.

3. An intraseasonal GPI measuring intraseasonal variation of TC genesis potential

a. *Candidate factors*

In addition to the factors used in ENGPI, we consider six additional potential factors: relative vorticity at 850 hPa weighted by the Coriolis parameter $f\zeta_{r850}$, vertical pressure velocity at 500 hPa ω_{500}, meridional gradient of zonal wind at 500 hPa U_{y500}, zonal gradient of zonal wind at 850 hPa U_{x850}, the vertical shear of zonal winds between 200 and 850 hPa V_{zs}, and SST anomaly relative to tropical (30°S–30°N) mean SST_a. All 10 candidate factors are listed in Table 1. Why do we implement six new factors? Using $f\zeta_{r850}$ is based on the following considerations. First, the absolute vorticity used in ENGPI is a sum of the Coriolis parameter

TABLE 1. Candidate large-scale environmental factors.

Factor	Description
V_{pot}	Maximum potential intensity ($m\,s^{-1}$)
SST_a	SST anomaly relative to tropical (30°S–30°N) mean SST (K)
RH_{600}	Relative humidity at 600 hPa (%)
U_{x850}	Zonal gradient of zonal wind at 850 hPa (s^{-1})
U_{y500}	Meridional gradient of zonal wind at 500 hPa (s^{-1})
V_{zs}	Zonal component of vertical wind shear between 200 and 850 hPa ($m\,s^{-1}$)
V_s	Total vertical wind shear between 200 and 850 hPa ($m\,s^{-1}$)
$f\zeta_{r850}$	Relative vorticity at 850 hPa weighted by the Coriolis parameter (s^{-2})
η_{850}	Absolute vorticity at 850 hPa (s^{-1})
ω_{500}	Vertical pressure velocity at 500 hPa ($Pa\,s^{-1}$)

f and relative vorticity ζ_{r850}. In the off-equatorial TC genesis region, the value of the Coriolis parameter can be significantly larger than the relative vorticity, and thus the effect of relative vorticity may be overshadowed by the Coriolis parameter. Second, an important role of the Coriolis parameter is to reduce the genesis potential for TC being created near the equator. Using f as a multiplier would reduce GPI near the equator and amplify the role of relative vorticity at higher latitudes. The physical meaning of the $f\zeta_{r850}$ may be understood in terms of the vorticity equation. In the vorticity equation, the divergence term $-(f+\zeta_{r850})D$ represents vorticity generation. In the off-equatorial region, the convergence $-D$ is roughly proportional to ζ_{r850} (Charney and Eliassen 1964) and the absolute vorticity $f+\zeta_{r850}$ tends to be dominated by f. Thus, the generation term $-(f+\zeta_{r850})D$ can be approximated by $f\zeta_{r850}$. The ω_{500} is shown to be a meaningful factor in the North Atlantic (Murakami and Wang 2010). The 500-hPa vorticity resulting from meridional shear of zonal winds was suggested to be important in the western North Pacific TCG (Fu et al. 2012; Peng et al. 2012). Different from the total vertical wind shear, the vertical shear of zonal wind distinguishes the easterly and westerly vertical shear. The easterly vertical shear, differing from a westerly vertical shear, may favor destabilization of synoptic waves and TC development (Wang and Xie 1996; Xie and Wang 1996) when its amplitude is not too large. The relative SST anomaly is used because previous studies have shown that the North Atlantic basin total TC genesis is robustly correlated with the relative SST anomalies in observations (Latif et al. 2007; Swanson 2008; Vecchi et al. 2008; Villarini and Vecchi 2012) and in dynamical models (Zhao et al. 2010; Murakami et al. 2012; Knutson et al. 2013).

Analysis of the linear correlation between TCG frequency and each individual factor reveals that the highest correlation with observed TCG frequency is the $f\zeta_{r850}$ ($r=0.73$), and the second highest is ω_{500} ($r=-0.66$) (Table 2). Among the four factors (V_{pot}, η_{850}, RH_{600}, and V_s) related with ENGPI, the RH_{600} has highest correlation with TCG frequency ($r=0.55$). This explains why Camargo et al. (2009) found RH_{600} has primary contribution to TCG frequency on intraseasonal time scale. The total vertical shear V_s is nearly independent of TCG frequency. Intriguingly, V_{pot} and SST_a are negatively correlated with TCG frequency, which are opposite to their contributions to climatological ENGPI. These results indicate that V_s and V_{pot}, which are good for predicting climatological TCG potential, are not applicable to intraseasonal variability of TCG.

b. Intraseasonal GPI

Different from using the total field variable in ENGPI, we focus on anomalous large-scale environmental factors that generate anomalous TCG frequency on intraseasonal time scale. To derive an anomalous GPI, we used stepwise regression to select significant factors and obtain an optimum combination of multifactors. The relative importance of each candidate factor was measured by the order in which a factor was selected.

TABLE 2. Correlation coefficients among nine candidate factors and the tropical cyclone genesis frequency (TCGF) as well as between any two candidate factors. The boldface numbers indicate absolute value is greater than 0.5. Sample size is 248.

(20°S–0°)	TCGF	V_{pot}	SST_a	RH_{600}	U_{x850}	U_{y500}	V_{zs}	V_s	$f\zeta_{r850}$	ω_{500}
TCGF	1.00	−0.28	−0.14	**0.55**	−0.25	**−0.54**	−0.42	−0.01	**0.73**	**−0.66**
V_{pot}	−0.28	1.00	0.47	0.04	−0.29	0.30	**0.71**	−0.01	**−0.53**	0.11
SST_a	−0.14	0.47	1.00	0.26	−0.42	0.42	0.35	−0.06	−0.39	−0.14
RH_{600}	**0.55**	0.04	0.26	1.00	**−0.75**	−0.18	−0.14	0.05	0.33	**−0.92**
U_{x850}	−0.25	−0.29	−0.42	**−0.75**	1.00	−0.08	−0.20	0.01	0.09	**0.66**
U_{y500}	**−0.54**	0.30	0.42	−0.18	−0.08	1.00	**0.51**	−0.06	**−0.80**	0.25
V_{zs}	0.42	**0.71**	0.35	−0.14	−0.20	**0.51**	1.00	−0.03	**−0.75**	0.26
V_s	−0.01	−0.01	−0.06	0.05	0.01	−0.06	−0.03	1.00	0.03	−0.01
$f\zeta_{r850}$	**0.73**	**−0.53**	−0.39	0.33	0.09	**−0.80**	**−0.75**	0.03	1.00	**−0.50**
ω_{500}	**−0.66**	0.11	−0.14	**−0.92**	**0.66**	0.25	0.26	−0.01	**−0.50**	1.00

TABLE 3. Results of stepwise selection of the influential factors for each MJO (OLR) index obtained from latitude ranges of 30°S–30°N, 20°S–20°N, 15°S–15°N, 15°S–0°, 20°S–0°, and 30°S–0°. The values indicate complex correlation coefficients. The numbers in parentheses indicate the order of selection. The best index based on results is in boldface.

MJO (OLR) index	V_{pot}	SST_a	RH_{600}	U_{x850}	U_{y500}	V_{zs}	V_s	$f\zeta_{r850}$	ω_{500}
30°S–30°N	—	—	—	—	—	0.752 (3)	—	0.743 (2)	0.643 (1)
20°S–20°N	—	—	—	—	—	0.757 (3)	—	0.645 (1)	0.748 (2)
15°S–15°N	—	—	—	—	—	0747 (3)	—	0.653 (1)	0.739 (2)
15°S–0°	—	—	—	—	—	0.786 (3)	—	0.701 (1)	0.778 (2)
20°S–0°	—	—	—	—	—	**0.811 (3)**	—	**0.726 (1)**	**0.802 (2)**
30°S–0°	—	—	—	—	—	0.803 (3)	—	0.701 (1)	0.792 (2)

Table 3 summarizes the results of selected factors by the stepwise regression. The final selection of significant factors and the corresponding regressed equation is

$$\mathrm{ISGPI} = 0.682 f\zeta_{r850} + (-0.366)\omega_{500} + 0.188 V_{zs}. \qquad (2)$$

Equation (2) contains only three dynamic factors that measure the likelihood of anomalous TCG on a 20–70-day time scale; thus, it is called an intraseasonal GPI. In Eq. (2), the ISGPI and each factor are normalized by their corresponding standard deviation so that the regression coefficients for each factor reflect their relative contribution to the ISGPI. The $f\zeta_{r850}$ has the highest contribution and its weight is nearly twice larger than ω_{500}. The vertical shear of zonal winds V_{zs} is significantly correlated with TCG frequency ($r = -0.42$) and complementary to or relatively independent of $f\zeta_{r850}$ and ω_{500} (Table 2). It was selected by the F test, but its independent contribution to ISGPI is small. While the thermodynamic factor RH_{600} has a higher correlation with TCG frequency than V_{zs}, it was not selected because the RH_{600} is highly correlated with ω_{500} ($r = -0.92$) and its effect can largely be surrogated by ω_{500}. Physically, a humid environment often occurs when midlevel upward motion exists.

The sensitivity tests have been carried out with regard to the choice of MJO (OLR) index. Table 3 shows that the conclusions presented in this work are robust no matter how the OLR MJO index is defined. However, the OLR index defined between 0° and 20°S yields the best results, suggesting that the climatological information (variance distribution) used to define the OLR index helps optimize the ISGPI. Parallel computations have also been done using the RMM index and velocity potential $\Delta\chi_{850-150}$ index (Adames and Wallace 2014) to see the sensitivity of the ISGPI to the choice of three MJO indices (Table 4 and Fig. 3). The results suggest that the ISGPI established using the simple OLR index (0°–20°S) is the best. As shown in Fig. 3, the ISGPI faithfully represents the anomalous TCG frequency associated with MJO evolution with a correlation coefficient of 0.81. This may be because both the RMM index and velocity potential index are defined using equatorial symmetric latitude bands across all seasons, while the OLR MJO index includes the effect of the seasonal variation of basic state on MJO.

4. Discussion: Mechanisms by which MJO modulates TC genesis

How MJO affects TCG in global oceans during austral summer remains an unresolved issue. Camargo et al. (2009) found the midlevel humidity is the major contributor. This is partially confirmed by our analysis. However, thinking beyond the four factors that control the annual cycle of TCG, we found the intraseasonal variability of TCG is most effectively controlled by the low-level relative vorticity.

To elaborate this point, let us examine the low-level (850 hPa) horizontal circulation structure of the MJO (Fig. 4). When the MJO convection center is located in the equatorial Indian Ocean (90°E), the regressed MJO 850-hPa winds exhibit a coupled Kelvin–Rossby wave

TABLE 4. Results of stepwise selection of the influential factors for three MJO indices: OLR index (0°–20°S range), the Adames and Wallace (2014) index (90°S–90°N range) using global velocity potential difference between 850 and 150 hPa, and the Wheeler and Hendon (2004) RMM index using OLR, U850, and U200 averaged over 15°S–15°N. The values indicate complex correlation coefficients. The numbers in parentheses indicate the order of selection.

MJO index	V_{pot}	SST_a	RH_{600}	U_{x850}	U_{y500}	V_{zs}	V_s	$f\zeta_{r850}$	ω_{500}
OLR (0°–20°S)	—	—	—	—	—	0.811 (3)	—	0.726 (1)	0.802 (2)
$\Delta\chi_{850-150}$ (90°S–90°N)	—	—	—	0.679 (3)	—	—	—	0.671 (2)	0.633 (1)
RMM, using OLR, U850, and U200 (15°S–15°N mean)	—	—	—	—	—	—	—	0.706 (2)	0.607 (1)

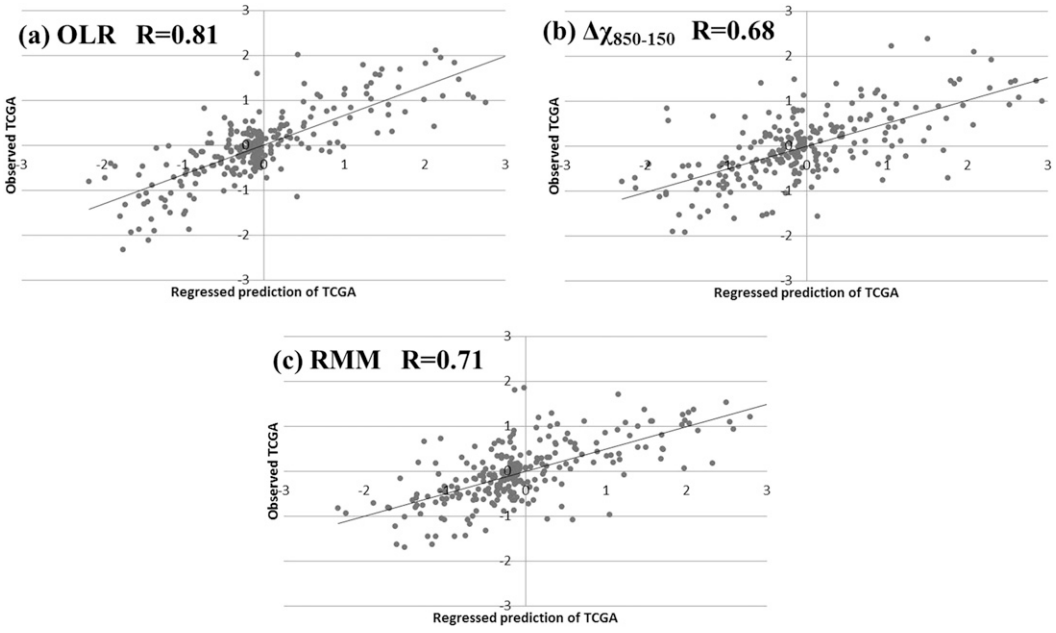

FIG. 3. Comparison of TCG prediction skill using different MJO indices. Shown are the scattered diagrams of normalized regressed prediction of TCG anomaly and the observed TCG anomaly using (a) OLR (0°–20°S), (b) $\Delta\chi_{850-150}$ (90°S–90°N), and (c) the RMM index (using OLR, U850, and U200 averaged over 15°S–15°N).

structure: to the west of the MJO convection is a Rossby wave component featured by a pair of cyclonic gyres residing on each side of the equator, with strong equatorial westerlies in between, and to the east of the MJO convection is a Kelvin wave component featured by equatorial easterlies and a low pressure anomaly. This coupled Kelvin–Rossby wave structure is similar to a Gill (1980) pattern, but they are not the same. The zonal extent ratio of the Kelvin easterly versus Rossby westerly is 2.1 in MJO, but it is 3.0 in the Gill pattern. The relative strength of the maximum Rossby westerly speed versus maximum Kelvin easterly speed averaged over 5°S and 5°N is 0.9 in MJO, but it is 2.2 in the Gill pattern (Wang et al. 2016). The structural differences between the Gill pattern and the MJO arise from the nature of the precipitation heating. In the Gill pattern the heating is specified and waves are passive responses, while in the MJO dynamics the heating is interactive with the waves and the waves can feedback to the heating (Wang et al. 2016).

Note that the structure shown in Fig. 4 is nearly symmetric about the equator because the MJO convection was selected to be centered at the equator (90°E). In our analysis of austral summer MJO, we used the latitude band 0°–20°S to define evolution of MJO convection; therefore, the regressed MJO winds at 850 hPa shown in Fig. 5 (top panels), for both phase 3 (when the MJO convection is centered over the Indian Ocean; 10°S, 90°E) and phase 5 (when the MJO convection is centered over the Maritime Continent; 10°S, 130°E), display equatorial asymmetric structure with equatorial zonal winds shifted toward the SH. This is because during austral summer, the tropical convergence zone and associated easterly total vertical shear (monsoon total vertical shear) are shifted to the SH, and as a result, the MJO structure also changes and exhibits an equatorial asymmetry with the SH Rossby gyres being enhanced and the Northern

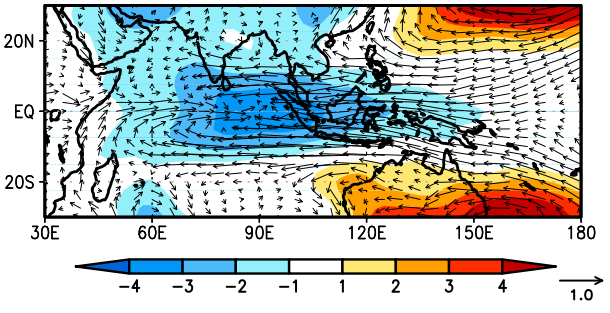

FIG. 4. The observed MJO low-level horizontal structure: 850-hPa wind (m s^{-1}; vectors) and 850-hPa zonal wind speed (m s^{-1}; shading). The structure is obtained by regressing the 20–70-day bandpass-filtered fields with reference to the convective anomaly in the equatorial Indian Ocean averaged over 10°S–10°N, 80°–100°E. The wind strengths are scaled to a fixed 3 mm day^{-1} precipitation rate.

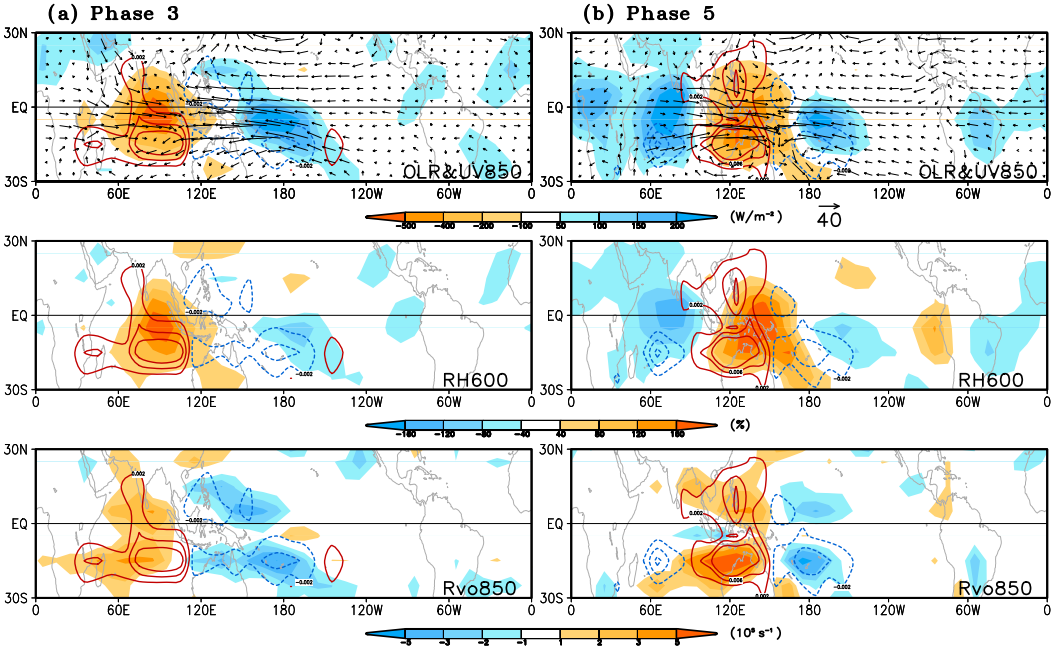

FIG. 5. Composite maps for intraseasonal anomalies of (top) OLR with 850-hPa wind vector ($m\,s^{-1}$), (middle) relative humidity at 600 hPa, and (bottom) cyclonic relative vorticity at 850 hPa for (a) phase 3 and (b) phase 5 of the MJO evolution during austral summer (NDJFMA) of 1979–2014. The TCG frequency anomaly (TC number per day) is plotted with contours. Relative vorticity is scaled by 10^5.

Hemisphere (NH) counterpart weakened (Fig. 5, top). This latitudinal asymmetry is primarily induced by the effect of the total vertical wind shear of the seasonal mean flow because, in theory, the presence of large-scale total vertical wind shears can markedly change the structure of the Rossby wave response, making it stronger in the hemisphere where easterly total vertical shear exists while weaker in the hemisphere where westerly total vertical shear resides (Wang and Xie 1996; Xie and Wang 1996). This theoretical result has been confirmed by numerical experiments (Wang et al. 2003). The theory explains the equatorial asymmetric structures of the 850-hPa winds seen in Fig. 5, especially at phase 5.

When the MJO convection (negative OLR) center is located over the Indian Ocean (phase 3), the midlevel humidity RH_{600} has its maximum located near but slightly south of the equator (Fig. 5a, middle). On the other hand, the relative vorticity field shows an off-equatorial cyclonic vorticity center at 15°S associated with the Rossby cyclonic gyre to the west of the MJO convection and an off-equatorial anticyclonic vorticity center at 15°S accompanying the Kelvin wave easterly to the east of the convection center (Fig. 5a, bottom). This MJO structure is consistent with Fig. 1 of Wang et al. (2016). In their three-dimensional schematic MJO structure, the maximum convection center and RH_{600} (pattern correlation coefficient between convection and RH_{600} is 0.8) is located at the equator and to the east of low-level off-equatorial cyclonic vorticities in both hemispheres. Evidently, the relative vorticity is better indicative of where TCG occurs in terms of latitudinal locations. When the MJO convection center moves over the Maritime Continent (phase 5), the RH_{600} centers remain near the equator although the positive anomalies tend to extend southward (Fig. 5b, middle). The relative vorticity still better matches the TCG frequency in latitudinal locations. In the zonal direction, the cyclonic/anticyclonic shear vorticity regions tend to coincide with positive and negative TCG anomalies better than the RH_{600} anomalies. The latter have an evident eastward phase shift with the TCG anomalies. The results in Fig. 5 explain why the MJO relative vorticity is better related to TCG anomaly than the midlevel relative humidity in general.

In sum, the MJO enhances (suppresses) TC genesis primarily through its low-level westerly (easterly) anomaly that induces cyclonic (anticyclonic) shear vorticity. In the off-equatorial region, the boundary layer Ekman pumping is primarily controlled by the relative vorticity at the top of the boundary layer (Charney and Eliassen 1964). Thus, 850-hPa cyclonic (anticyclonic) vorticity induces upward (downward) motion that

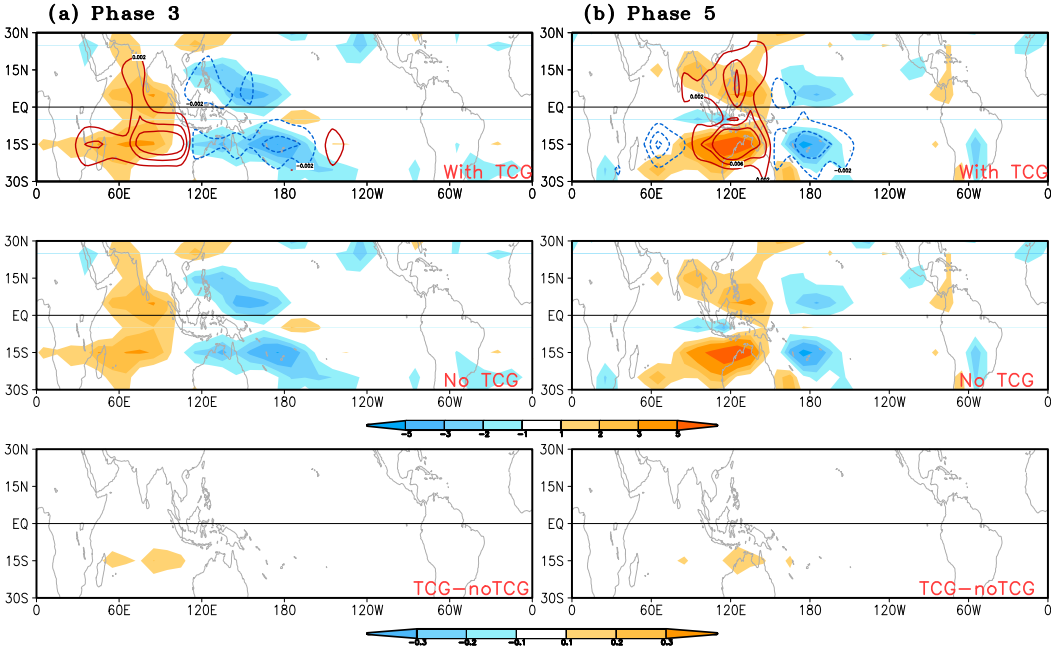

FIG. 6. Testing the impact of the TCG on MJO relative vorticity. Composite maps for intraseasonal anomalies of cyclonic relative vorticity (s^{-1}) at 850 hPa for (a) phase 3 and (b) phase 5 of the MJO evolution (top) with TCG, (middle) without TCG, and (bottom) their difference during austral summer (NDJFMA) of 1979–2014. The TCG frequency anomaly (TC number per day) is plotted with contours. Relative vorticity is scaled by 10^5.

moistens (dries) the lower troposphere, leading to increased (decreased) TCG frequency.

Since the MJO relative vorticity at 850 hPa plays the major role in regulating TCG, one may wonder how important the TCG influence is on the MJO relative vorticity. Since the probability of the TCG occurrence is very small (~0.04 in five days for a 5° × 5° grid) and the relative vorticity of TC in its genesis stage is also small, we anticipate that the relative vorticity of the TCG is negligibly small compared to the relative vorticity associated with the MJO. To test this idea, we have diagnosed the possible impact of relative vorticity by the TC itself to the relationship between intraseasonal relative vorticity and cyclogenesis activities. Using the same method as in Camargo et al. (2009), composite anomalies of intraseasonal relative vorticity at 850 hPa are prescribed as zero where the TCG occurred. Figure 6 is similar to Fig. 5, but with and without the impact of a TC. As we can see, the difference in relative vorticity at the TCG location is small, which may not affect the results.

5. Performance of the ISGPI in representing MJO regulation of TC genesis

Here we show how the ISGPI reproduces the MJO modulation of TCG in comparison with the ENGPI. Since the ENGPI is developed for the total field, we first computed total GPI using daily total values (daily climatology plus MJO anomaly). Then the GPI anomaly on the MJO time scale (hereafter MJO ENGPI for short) is obtained by removing the GPI climatology (computed using daily climatology values) from the total GPI; namely, MJO ENGPI = total ENGPI − climatological ENGPI.

Since one of our objectives aims at predicting the SH TC genesis potential associated with the MJO, we want to first assess the performance of ISGPI and ENGPI in reproducing the TCG anomalies over the primary TC genesis zone in the SH between 10° and 20°S (Fig. 1b). Figure 7 shows the TCG frequency along the primary TCG zone for the composite eight phases of the MJO along with the corresponding ISGPI and ENGPI. The observed TCG frequency exhibits a systematic eastward migration of the TCG maximum from 60°E for phase 1 to 160°W for phase 8. Overall, the eastward propagation of TCG maximum is captured by the ISGPI remarkably well as evidenced by the high pattern correlation coefficient (PCC) between the ISGPI and TCG frequency at each phase. The eight-phase-averaged PCC skill is 0.86. The ENGPI also shows an eastward propagation consistent with the TCG frequency but with a significantly lower averaged PCC score of 0.67. The

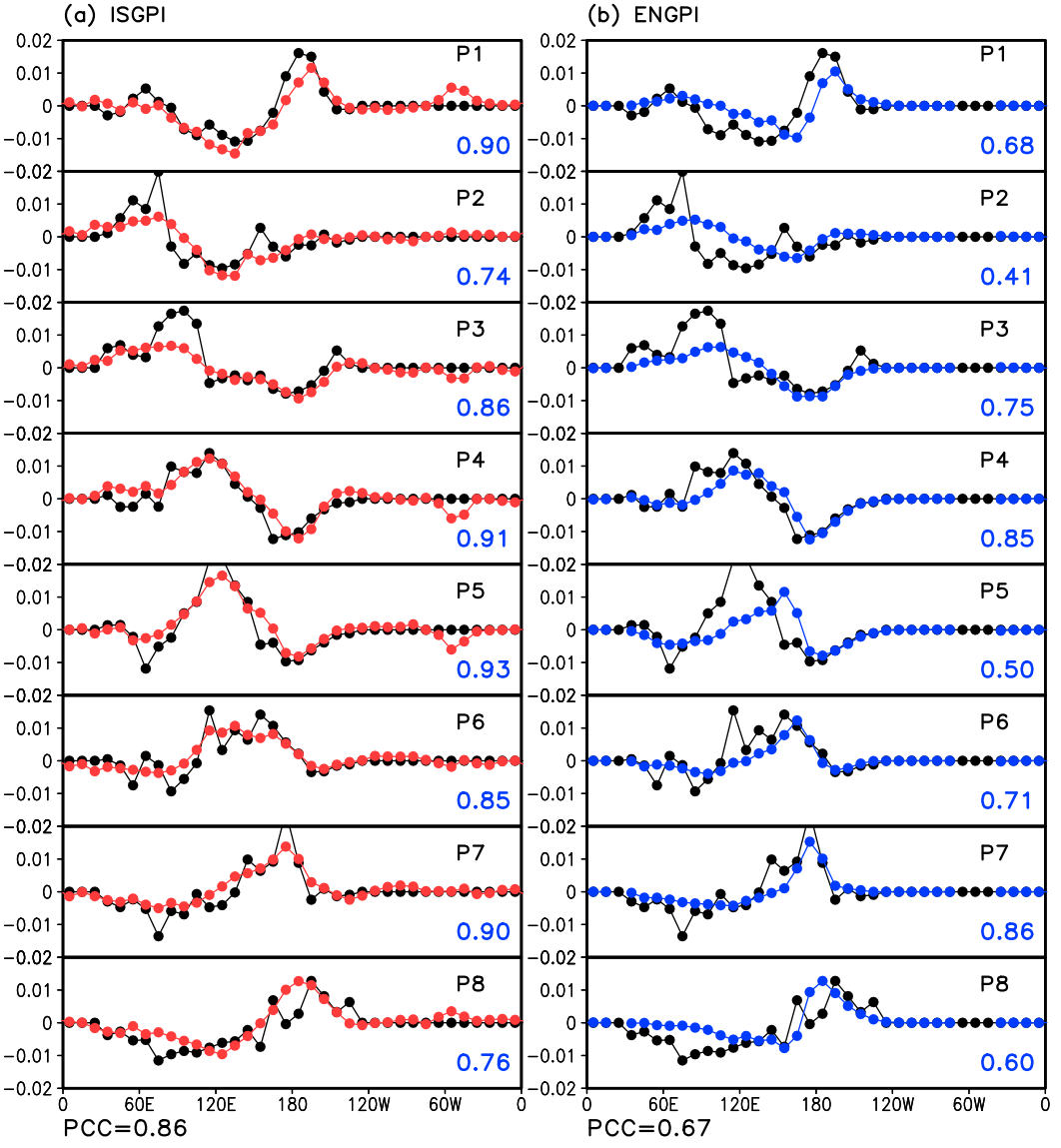

FIG. 7. Performance of the (a) ISGPI (red curves) and (b) ENGPI (blue curves) in reproducing observed TCG frequency (black curves) along the major TCG zone of Southern Ocean between 10° and 20°S during composite eight phases (P1–P8) in austral summer (NDJFMA) of 1979–2014 (TC number per day). The numbers at the bottom-right corner of each panel indicate the PCC between each GPI and observed TCG anomaly. The average PCCs for the eight phases in (a) and (b) are shown at the bottom.

maximum (minimum) ISGPI corresponds very well to the observed maximum (minimum) TCG occurrences, but the ENGPI has some phase discrepancies with observations, notably for phases 2 and 5, which is due to the phase shift between RH_{600} and TCG frequency as shown by Fig. 5b.

In austral summer, TC forecast over the Australian region and several southern islands in the Indian and South Pacific Oceans are very important for local hazard management. For this purpose, in Fig. 8 we show how useful the ISGPI is in representing TCG in three subregions of SH. The TCG numbers in these three regions vary markedly with the phases of MJO propagation, indicating the fundamental roles of MJO in controlling TCG in each region of the SH. The ISGPI captures this MJO regulation realistically over all three regions. In the southern Indian Ocean (SIO; 50°–100°E), TCG frequency peaks at phase 3 (when MJO convection center is at 90°E), while in the Australian region (AUS; 100°–150°E), TCG frequency reaches a maximum at phase 5 (when MJO convection center is at 135°E), and farther east in the South

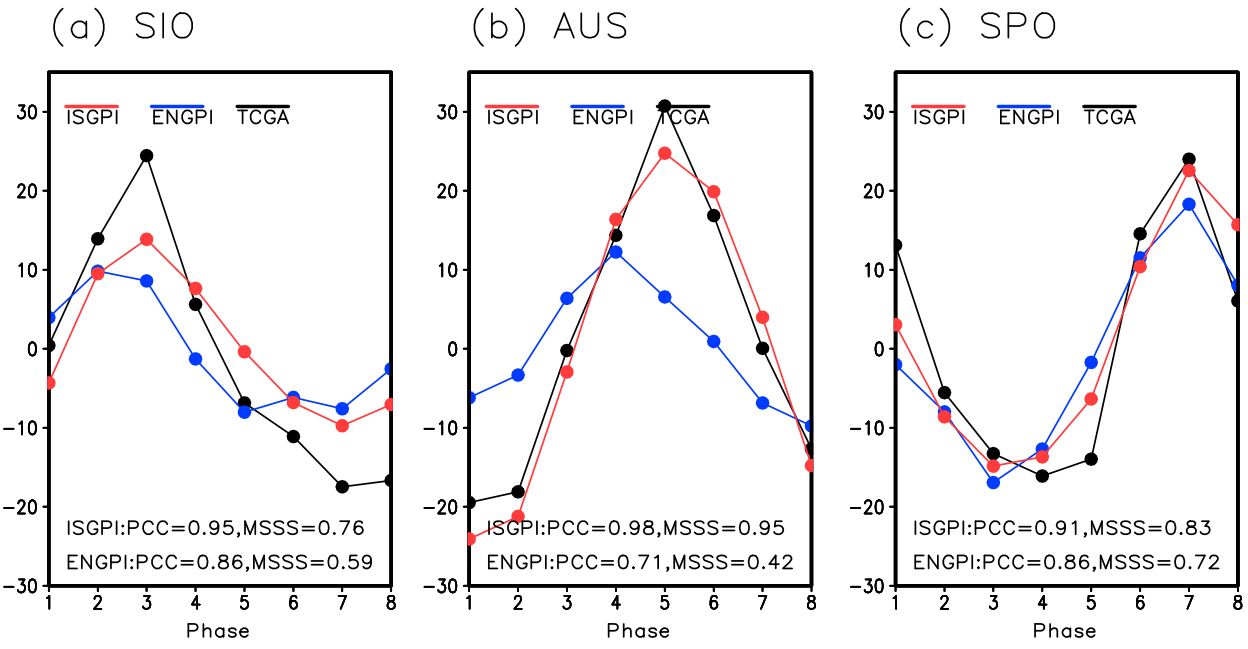

FIG. 8. Performance of the ISGPI (red curves) and ENGPI (blue curves) in reproducing observed TCG number (y axis; black curves) in three subregions of the Southern Ocean: (a) SIO (10°–20°S, 50°–100°E), (b) AUS (10°–20°S, 100°–150°E), and (c) SPO (10°–20°S, 150°E–160°W) during composite eight phases (P1–P8) of MJO in austral summer (NDJFMA) of 1979–2014. The PCC and MSSS for ISGPI and ENGPI are shown at the bottom of each panel.

Pacific Ocean (SPO; 150°E–160°W) it peaks at phase 7 (when MJO convection center is at 180°). The eastward propagation of the MJO is obviously the pacemaker for the eastward shift of the maximum TCG locations in the three subregions. The ISGPI almost exactly captures both the maximum and minimum TCG phases at each subregion, but the ENGPI tends to have its maximum and minimum phases occurring one phase earlier than the observed counterpart. This is because the ENGPI heavily relies on RH_{600}, which tends to have an eastward phase shift with TCG frequency as shown in Fig. 5b. Overall, both the mean-square skill score (MSSS) and PCC skills of ISGPI are significantly higher than the corresponding counterparts of the ENGPI over the Australian region and SIO (Fig. 8).

To show the MJO regulation of TC genesis over the entire tropics, we present, in Fig. 9, the observed TCG frequency anomalies (shading) and the corresponding ISGPI (Fig. 9, left) and ENGPI (Fig. 9, right). The ISGPI pattern matches the observed TC genesis pattern well with the PCC ranging from 0.63 to 0.71 at various phases, and the averaged PCC skill is 0.68. This skill is significantly higher than that obtained by using ENGPI (averaged PCC = 0.52). In NH, the ISGPI matches observation much better than the ENGPI, which tends to have too-weak signals. In SH, the ISGPI better matches observation than the ENGPI, which tends to have a phase shift with observed TCG frequency. The latter problem was seen before in Fig. 8.

6. Summary

Our study of intraseasonal variations of TC genesis during 35 austral summers (from November to the next April) reveals that the low-level (850 hPa) relative vorticity weighted by the Coriolis parameter $f\zeta_{r850}$ is the most effective large-scale controlling factor for TCG and that the midtropospheric vertical motion is a second complementary factor (Table 2). The MJO modulates TC genesis primarily through its Rossby wave gyres and meridional shears of the equatorial zonal winds (Fig. 5). The MJO-induced off-equatorial low-level cyclonic (anticyclonic) vorticity anomalies generate upward (downward) motion and humidify (dry) the lower troposphere, thereby enhancing (suppressing) TC genesis.

We proposed an intraseasonal GPI to quantify MJO's modulation of TC genesis [Eq. (2) and Fig. 3a]. The ISGPI can quantify intraseasonal variability of TC genesis potential on each phase of the MJO (correlation skill r = 0.86; Fig. 7) and the intraseasonal evolution of TCG frequency in each subregion of the SH ocean, including the southern Indian Ocean (r = 0.95; MSSS = 0.76), the Australian monsoon ocean region (r = 0.98;

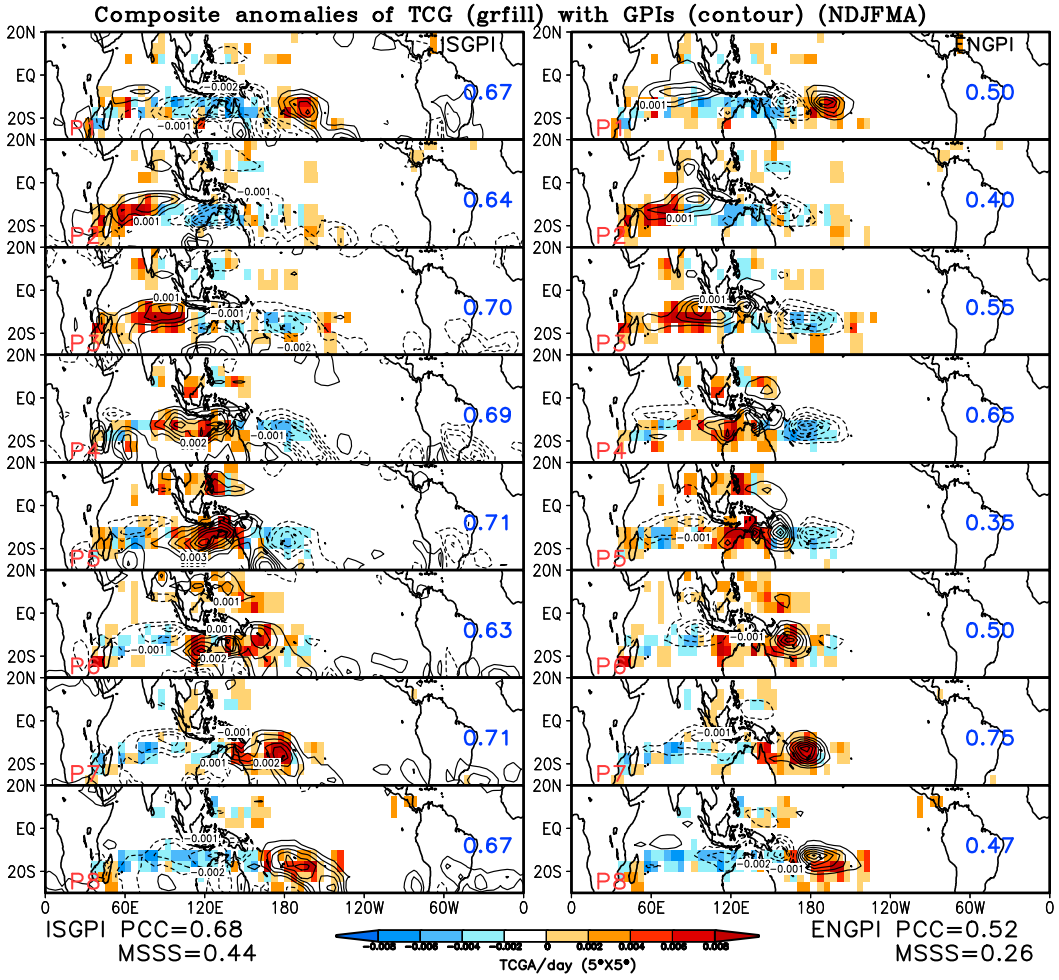

FIG. 9. Performance of the (left) ISGPI (contours) and (right) ENGPI (contours) in reproducing observed TCG frequency (color shading) in the tropics during composite eight phases (P1–P8) in austral summer (NDJFMA) of 1979–2014. The TCG frequency is computed for each day and each 5° × 5° grid. The numbers at the bottom-right corner of each panel indicate the PCC between each GPI and observed TCG anomaly. The average PCC and MSSS for the eight phases of ISGPI and ENGPI are shown at the bottom.

MSSS = 0.95), and the South Pacific (r = 0.91; MSSS = 0.83) (Fig. 8), as well as in the entire tropical region (Fig. 9). As such, the skill of the new ISGPI is markedly higher than the climatological GPI (ENGPI) in describing intraseasonal variability of TCG potential.

Application of the new ISGPI may have a large potential to improve subseasonal prediction of TC genesis because the SH TC genesis is remarkably modulated by the MJO. For instance, along the SH TC genesis zone (10°–20°S), there are the three hottest spots of TCG, located in the central SIO (70°–80°E), northwest of Australia (110°–120°E), and near the date line in SPO (170°E–180°). Near the date line in the SPO, the probability of TCG at the wettest phase is 3.5 times of the climatological value while in the driest phase it decreases to 20% of the climatological value (Fig. 10). The ratio of TCG probability between the wettest and driest phases of MJO is 19. Similarly, this ratio is 11 over the SIO and 5 over the northwest of Australia. Notably, these remarkable modulations are captured quite well by the ISGPI. This suggests that if dynamical models can faithfully predict large-scale low-level vorticity and 500-hPa vertical motion anomalies associated with the MJO, use of ISGPI can potentially make useful TCG probabilistic prediction.

The results of the present study imply that the large-scale factors controlling TCG may differ on various time scales. Those factors that control the annual variation of TCG may not equally apply to other time scales such as intraseasonal or interannual–decadal time scales. Further studies are required for fully understanding the relationship

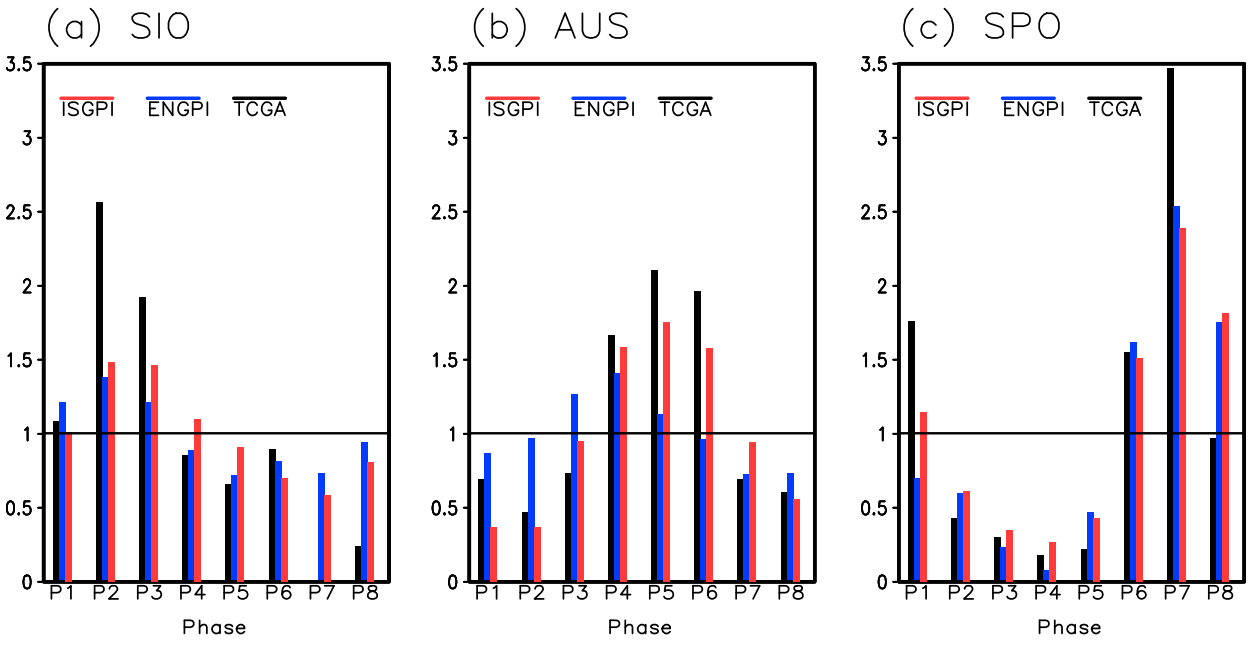

FIG. 10. The normalized TCG frequency (by its corresponding climatological mean TCG frequency) derived from observation (black bars) and predicted by ISGPI (red bars) and ENGPI (blue bars) at three hot spots of the TCG zone in the Southern Hemisphere: (a) SIO (10°–20°S, 70°–80°E), (b) AUS (10°–20°S, 110°–120°E), and (c) SPO (10°–20°S, 170°E–180°) during composite eight phases (P1–P8) of MJO in austral summer (NDJFMA) of 1979–2014.

between environmental conditions and TC genesis on various time scales and in the future scenario under anthropogenic forcing.

The present results also suggest that, in order for a general circulation model to simulate realistic impacts of the MJO on TCG, a model must reproduce realistic eastward propagation and the low-level circulation structure of the MJO. The latter has not been paid enough attention in the modeling community. We stress that both the dynamical model-simulated MJO low-level circulation structure and its eastward propagation are critically important in determining its impact on TC genesis.

The present study considered only the MJO modulation of TC genesis and neglected the upscale feedback from TC activity to the MJO. The latter needs to be further assessed. However, given the tiny climatological probability of TCG, this feedback effect might not have a significant impact on the results presented here.

Acknowledgments. This work was supported by the NSF Award AGS-1540783, NOAA Award NOAA/CVP NA15OAR4310177, the National Natural Science Foundation of China (Grant 41420104002), and the National Research Foundation of Korea (NRF) through a Global Research Laboratory (GRL) Grant (MEST 2011-0021927). The authors thank Dr. Bing Fu and Dr. Hiroyuki Murakami for providing the datasets and calculation program.

REFERENCES

Adames, A. F., and J. M. Wallace, 2014: Three-dimensional structure and evolution of the MJO and its relation to the mean flow. *J. Atmos. Sci.*, **71**, 2007–2026, doi:10.1175/JAS-D-13-0254.1.

Aiyyer, A., and J. Molinari, 2008: MJO and tropical cyclogenesis in the Gulf of Mexico and eastern Pacific: Case study and idealized numerical modeling. *J. Atmos. Sci.*, **65**, 2691–2704, doi:10.1175/2007JAS2348.1.

Barrett, B. S., and L. M. Leslie, 2009: Links between tropical cyclone activity and Madden–Julian oscillation phase in the North Atlantic and northeast Pacific basins. *Mon. Wea. Rev.*, **137**, 727–744, doi:10.1175/2008MWR2602.1.

Bessafi, M., and M. C. Wheeler, 2006: Modulation of south Indian Ocean tropical cyclones by the Madden–Julian oscillation and convectively coupled equatorial waves. *Mon. Wea. Rev.*, **134**, 638–656, doi:10.1175/MWR3087.1.

Camargo, S. J., K. A. Emanuel, and A. H. Sobel, 2007: Use of genesis potential index to diagnose ENSO effects on tropical cyclone genesis. *J. Climate*, **20**, 4819–4834, doi:10.1175/JCLI4282.1.

——, M. C. Wheeler, and A. H. Sobel, 2009: Diagnosis of the MJO modulation of tropical cyclogenesis using an empirical index. *J. Atmos. Sci.*, **66**, 3061–3074, doi:10.1175/2009JAS3101.1.

Chand, S. S., and K. J. E. Walsh, 2010: The influence of the Madden–Julian oscillation on tropical cyclone activity in the Fiji region. *J. Climate*, **23**, 868–886, doi:10.1175/2009JCLI3316.1.

Charney, J. G., and A. Eliassen, 1964: On the growth of the hurricane depression. *J. Atmos. Sci.*, **21**, 68–75, doi:10.1175/1520-0469(1964)021<0068:OTGOTH>2.0.CO;2.

Dee, D. P., and Coauthors, 2011: The ERA-Interim reanalysis: Configuration and performance of the data assimilation system. *Quart. J. Roy. Meteor. Soc.*, **137**, 553–597, doi:10.1002/qj.828.

Duchon, C. E., 1979: Lanczos filtering in one and two dimensions. *J. Appl. Meteor. Climatol.*, **18**, 1016–1022, doi:10.1175/1520-0450(1979)018<1016:LFIOAT>2.0.CO;2.

Efroymson, M. A., 1960: Multiple regression analysis. *Mathematical Methods for Digital Computers*, A. Ralston and H. S. Wilf, Eds., Wiley, 191–203.

Emanuel, K. A., and D. S. Nolan, 2004: Tropical cyclone activity and global climate. *26th Conf. on Hurricanes and Tropical Meteorology*, Miami, FL, Amer. Meteor. Soc., 10A.2. [Available online at https://ams.confex.com/ams/26HURR/techprogram/paper_75463.htm.]

Fu, B., M. S. Peng, and T. Li, 2012: Developing versus nondeveloping disturbances for tropical cyclone formation. Part II: Western North Pacific. *Mon. Wea. Rev.*, **140**, 1067–1080, doi:10.1175/2011MWR3618.1.

Gill, A. E., 1980: Some simple solutions for heat-induced tropical circulation. *Quart. J. Roy. Meteor. Soc.*, **106**, 447–462, doi:10.1002/qj.49710644905.

Hall, J. D., A. J. Matthews, and D. J. Karoli, 2001: The modulation of tropical cyclone activity in the Australian region by the Madden–Julian oscillation. *Mon. Wea. Rev.*, **129**, 2970–2982, doi:10.1175/1520-0493(2001)129<2970:TMOTCA>2.0.CO;2.

Jiang, X., M. Zhao, and D. E. Waliser, 2012: Modulation of tropical cyclones over the eastern Pacific by the intraseasonal variability simulated in an AGCM. *J. Climate*, **25**, 6524–6538, doi:10.1175/JCLI-D-11-00531.1.

Kikuchi, K., and B. Wang, 2010: Formation of tropical cyclones in the northern Indian Ocean associated with two types of tropical intraseasonal oscillation modes. *J. Meteor. Soc. Japan*, **88**, 475–496, doi:10.2151/jmsj.2010-313.

Kim, J.-H., C.-H. Ho, and H.-S. Kim, 2008: Systematic variation of summertime tropical cyclone activity in the western North Pacific in relation to the Madden–Julian oscillation. *J. Climate*, **21**, 1171–1191, doi:10.1175/2007JCLI1493.1.

Klotzbach, P. J., 2010: On the Madden–Julian oscillation–Atlantic hurricane relationship. *J. Climate*, **23**, 282–293, doi:10.1175/2009JCLI2978.1.

Knapp, K. R., M. C. Kruk, D. H. Levinson, H. J. Diamond, and C. J. Neumann, 2010: The International Best Track Archive for Climate Stewardship (IBTrACS): Unifying tropical cyclone best track data. *Bull. Amer. Meteor. Soc.*, **91**, 363–376, doi:10.1175/2009BAMS2755.1.

Knutson, T. R., and Coauthors, 2013: Dynamical downscaling projections of twenty-first-century Atlantic hurricane activity: CMIP3 and CMIP5 model-based scenarios. *J. Climate*, **26**, 6591–6617, doi:10.1175/JCLI-D-12-00539.1.

Krishnamohan, K. S., K. Mohanakumar, and P. V. Joseph, 2012: The influence of Madden–Julian oscillation in the genesis of north Indian Ocean tropical cyclones. *Theor. Appl. Climatol.*, **109**, 271–282, doi:10.1007/s00704-011-0582-x.

Latif, M., N. Keenlyside, and J. Bader, 2007: Tropical sea surface temperature, vertical wind shear, and hurricane development. *Geophys. Res. Lett.*, **34**, L01710, doi:10.1029/2006GL027969.

Li, R. C. Y., and W. Zhou, 2013: Modulation of western North Pacific tropical cyclone activity by the ISO. Part I: Genesis and intensity. *J. Climate*, **26**, 2904–2918, doi:10.1175/JCLI-D-12-00210.1.

Liebmann, B., and C. A. Smith, 1996: Description of a complete (interpolated) outgoing longwave radiation dataset. *Bull. Amer. Meteor. Soc.*, **77**, 1275–1277.

——, H. H. Hendon, and J. D. Glick, 1994: The relationship between tropical cyclones of the western Pacific and Indian Oceans and the Madden–Julian oscillation. *J. Meteor. Soc. Japan*, **72**, 401–412.

Madden, R., and P. Julian, 1971: Detection of a 40–50 day oscillation in the zonal wind in the tropical Pacific. *J. Atmos. Sci.*, **28**, 702–708, doi:10.1175/1520-0469(1971)028<0702:DOADOI>2.0.CO;2.

——, and ——, 1972: Description of global-scale circulation cells in the tropics with a 40–50 day period. *J. Atmos. Sci.*, **29**, 1109–1123, doi:10.1175/1520-0469(1972)029<1109:DOGSCC>2.0.CO;2.

Maloney, E. D., and D. L. Hartmann, 2000a: Modulation of eastern North Pacific hurricanes by the Madden–Julian oscillation. *J. Climate*, **13**, 1451–1460, doi:10.1175/1520-0442(2000)013<1451:MOENPH>2.0.CO;2.

——, and ——, 2000b: Modulation of hurricane activity in the Gulf of Mexico by the Madden–Julian oscillation. *Science*, **287**, 2002–2004, doi:10.1126/science.287.5460.2002.

Molinari, J., D. Knight, M. Dickinson, D. Vollaro, and S. Skubis, 1997: Potential vorticity, easterly waves, and eastern Pacific tropical cyclogenesis. *Mon. Wea. Rev.*, **125**, 2699–2708, doi:10.1175/1520-0493(1997)125<2699:PVEWAE>2.0.CO;2.

Murakami, H., and B. Wang, 2010: Future change of North Atlantic tropical cyclone tracks: Projection by a 20-km-mesh global atmospheric model. *J. Climate*, **23**, 2699–2721, doi:10.1175/2010JCLI3338.1.

——, and Coauthors, 2012: Future changes in tropical cyclone activity projected by the new high-resolution MRI-AGCM. *J. Climate*, **25**, 3237–3260, doi:10.1175/JCLI-D-11-00415.1.

Nakazawa, T., 1988: Tropical super clusters within intraseasonal variations over the western Pacific. *J. Meteor. Soc. Japan*, **66**, 823–839.

Peng, M. S., B. Fu, and T. Li, 2012: Developing versus nondeveloping disturbances for tropical cyclone formation. Part I: North Atlantic. *Mon. Wea. Rev.*, **140**, 1047–1066, doi:10.1175/2011MWR3617.1.

Ramsay, H. A., S. J. Camargo, and D. Kim, 2012: Cluster analysis of tropical cyclone tracks in the Southern Hemisphere. *Climate Dyn.*, **39**, 897–917, doi:10.1007/s00382-011-1225-8.

Swanson, K. L., 2008: Nonlocality of Atlantic tropical cyclone intensities. *Geochem. Geophys. Geosyst.*, **9**, Q04V01, doi:10.1029/2007GC001844.

Vecchi, G. A., K. L. Swanson, and B. J. Soden, 2008: Whither hurricane activity? *Science*, **322**, 687–689, doi:10.1126/science.1164396.

Ventrice, M. J., C. D. Thorncroft, and P. E. Roundy, 2011: The Madden–Julian oscillation's influence on African easterly waves and downstream tropical cyclogenesis. *Mon. Wea. Rev.*, **139**, 2704–2722, doi:10.1175/MWR-D-10-05028.1.

Villarini, G., and G. A. Vecchi, 2012: North Atlantic power dissipation index (PDI) and accumulated cyclone energy (ACE): Statistical modeling and sensitivity to sea surface temperature. *J. Climate*, **25**, 625–637, doi:10.1175/JCLI-D-11-00146.1.

Waliser, D. E., 2011: Predictability and forecasting. *Intraseasonal Variability of the Atmosphere–Ocean Climate System*, 2nd ed. W. K.-M. Lau and D. E. Waliser, Eds., Springer, 433–476.

——, and Coauthors, 2009: MJO simulation diagnostics. *J. Climate*, **22**, 3006–3030, doi:10.1175/2008JCLI2731.1.

Wang, B., and X. Xie, 1996: Low-frequency equatorial waves in vertically shear flow. Part I: Stable waves. *J. Atmos. Sci.*, **53**, 449–467, doi:10.1175/1520-0469(1996)053<0449:LFEWIV>2.0.CO;2.

——, and X. Zhou, 2008: Climate variation and prediction of rapid intensification in tropical cyclones in the western North Pacific. *Meteor. Atmos. Phys.*, **99**, 1–16, doi:10.1007/s00703-006-0238-z.

——, and G. S. Chen, 2016: A general theoretical framework for understanding essential dynamics of Madden–Julian oscillation. *Climate Dyn.*, doi:10.1007/s00382-016-3448-1.

——, and J.-Y. Moon, 2017: Sub-seasonal prediction of extreme weather events. *Bridging Science and Policy Implication for Managing Climate Extremes: Linking Science and Policy Implication*, C.-S. Chung and B. Wang, Eds., World Scientific, in press.

——, R. Wu, and T. Li, 2003: Atmosphere–warm ocean interaction and its impact on Asian–Australian monsoon variation. *J. Climate*, **16**, 1195–1211, doi:10.1175/1520-0442(2003)16<1195:AOIAII>2.0.CO;2.

——, F. Liu, and G. Chen, 2016: A trio-interaction theory for Madden-Julian oscillation. *Geosci. Lett.*, **3**, doi:10.1186/s40562-016-0066-z.

Wheeler, M. C., and H. H. Hendon, 2004: An all-season real-time multivariate MJO index: Development of an index for monitoring and prediction. *Mon. Wea. Rev.*, **132**, 1917–1932, doi:10.1175/1520-0493(2004)132<1917:AARMMI>2.0.CO;2.

Xie, X., and B. Wang, 1996: Low-frequency equatorial waves in vertically sheared zonal flows. Part II: Unstable waves. *J. Atmos. Sci.*, **53**, 3589–3605, doi:10.1175/1520-0469(1996)053<3589:LFEWIV>2.0.CO;2.

Zhang, C., 2013: Madden–Julian oscillation: Bridging weather and climate. *Bull. Amer. Meteor. Soc.*, **94**, 1849–1870, doi:10.1175/BAMS-D-12-00026.1.

Zhao, M., I. M. Held, and G. A. Vecchi, 2010: Forecasts of the hurricane season using a global atmospheric model assuming persistence of SST anomalies. *Mon. Wea. Rev.*, **138**, 3858–3868, doi:10.1175/2010MWR3366.1.